ELSEVIER

Computers & Geosciences 30 (2004) 249–258

COMPUTERS & GEOSCIENCES

www.elsevier.com/locate/cageo

TEMSPOL: a MATLAB thermal model for deep subduction zones including major phase transformations ☆

A.M. Negredo[a], J.L. Valera[a], E. Carminati[b,*]

[a] Department of Geophysics, Faculty of Physics, University Complutense of Madrid, Spain
[b] Department of Earth Sciences, University of Roma 'La Sapienza', P. le Aldo Moro 5, Roma I-00185, Italy

Received 27 January 2003; received in revised form 2 January 2004; accepted 5 January 2004

Abstract

TEMSPOL is an open MATLAB code suitable for calculating temperature and lateral anomaly of density distributions in deep subduction zones, taking into account the olivine to spinel phase transformation in a self-consistent manner. The code solves, by means of a finite difference scheme, the heat transfer equation including adiabatic heating, radioactive heat generation, latent heat associated with phase changes and frictional heating.

We show, with a few simulations, that TEMSPOL can be a useful tool for researchers studying seismic velocity, stress and seismicity distribution in deep subduction zones. Deep earthquakes in subducting slabs are thought to be caused by shear instabilities associated with the olivine to spinel phase transition in metastable olivine wedges. We investigate the kinematic and thermal conditions of the subducting plate that lead to the formation of metastable olivine wedges. Moreover, TEMSPOL calculates lateral anomalies of density within subducting slabs, which can be used to evaluate buoyancy forces that determine the dynamics of subduction and the stress distribution within the slab.

We use TEMSPOL to evaluate the effects of heat sources such as shear heating and latent heat release, which are neglected in commonly used thermal models of subduction. We show that neglecting these heat sources can lead to significant overestimation of the depth reached by the metastable olivine wedge.

Keywords: Temperature; Subduction; Phase transitions; Density anomaly; Olivine; Spinel

1. Introduction

Subcrustal earthquakes widely occur within subducting slabs. Shallow and intermediate events (depths <300 km) are likely produced by brittle fracturing and frictional sliding on pre-existing faults (Scholz, 1990) and possibly enhanced by dehydration embrittlement (Meade and Jeanloz, 1991). At depths >300 km, brittle and frictional processes are likely inhibited by enormous lithostatic pressures. Nevertheless, more than 20% of earthquakes with magnitude greater than 5 occur at depths greater than 300 km (Frohlich, 1989). Independent solutions to the paradox of the occurrence of deep earthquakes have been proposed by two groups of scientists on the basis of deformation experiments on germanate olivine and ice (Green et al., 1990; Kirby et al., 1991). According to both groups, deep earthquakes are caused by shear instabilities associated with olivine to spinel transformation. This phase transformation may be kinetically hindered in a cold slab descending into the mantle transition zone (e.g., Rubie, 1984), thus creating a wedge-shaped zone of metastable olivine that can persist down to about 660 km (Kirby et al., 1996). This might explain the occurrence of deep earthquakes and the largely recognised correlation of

☆ Code available from server at http://www.iamg.org/CGEditor/index.htm

*Corresponding author. Tel.: +39-6-49914950; fax: +39-6-4454729.

E-mail address: eugenio.carminati@uniroma1.it (E. Carminati).

0098-3004/$ - see front matter © 2004 Elsevier Ltd. All rights reserved.
doi:10.1016/j.cageo.2004.01.002

maximum depth of seismicity with the product of the age of the subducting lithosphere and the subduction velocity (e.g., Kirby et al., 1996).

Since olivine metastability is a temperature-controlled process, accurate and realistic thermal models of subduction zones are necessary for a better comprehension of deep seismicity. Moreover, temperature and phase changes are known to control density distribution within subducting slabs and consequently to influence the dynamics of subduction (Bina, 1996; Schmeling et al., 1999).

The role of subduction kinematics on the slab temperature distribution has been widely investigated with analytical (e.g., McKenzie, 1969) and numerical (e.g., Minear and Toksöz, 1970) thermal models since the early discovery of plate tectonics. We aim at improving important aspects of existing models and provide a useful tool for researchers studying deep subduction zones, with interests in seismology, metamorphism, seismic velocity distribution and dynamics of subduction zones. The purpose of this work is, therefore, to provide an open MATLAB code suitable for calculating temperature, density anomaly and mineral phases (olivine and spinel) distribution in deep subduction zones, taking into account phase transformations in a self-consistent manner. Our code is intended to be simple and easy to apply to real subduction zones. Moreover, we intend to evaluate the effects of heat sources such as radioactive or shear heating and latent heat release, which are neglected in commonly used thermal models (e.g., Stein and Stein, 1996).

2. Previous models

Among existing thermal models of deep subduction we can distinguish two different types of approach. Some models compute the temperature distribution only within the slab, which is assumed to descend in an isothermal (e.g., McKenzie, 1969) or in a adiabatically heated (e.g., Dässler and Yuen, 1996; Devaux et al., 1997, 2000) mantle. The influence of the surrounding mantle is accounted for as a boundary condition.

A second set of models (e.g., Minear and Toksöz, 1970; Toksöz et al., 1971; Turcotte and Schubert, 1973; Stein and Stein, 1996) includes mantle–slab thermal interactions and allows for the calculation of accurate temperature distributions in both slab and surrounding mantle. Minear and Toksöz (1970) and Toksöz et al. (1971) developed a numerical quasi-dynamic thermal model that included adiabatic heating, radioactive heat generation, phase changes and frictional heating. Stein and Stein (1996) further modified this model to introduce a temperature distribution of the oceanic lithosphere prior to subduction given by the plate model GDH1 (Stein and Stein, 1992). Despite this improvement, the model by Stein and Stein (1996) does not include shear or radiogenic heating or latent heat released during phase changes. This model is commonly used to investigate the conditions for the formation of metastable olivine wedges (Kirby et al., 1996) and the effects of buoyancy forces arising from density contrasts related to phase transformations (e.g., Bina, 1997; Marton et al., 1999). These models adopt a kinematic approach, i.e. a pre-defined velocity field is imposed. In contrast, dynamic models of subduction calculate the velocity field solving the coupled equations of conservation of mass, momentum and energy (e.g., Schmeling et al., 1999; Tezlaff and Schmeling, 2000), and include buoyancy forces due to phase transformation. Dynamic models are physically more self-consistent and provide a better understanding of subduction processes. However, they are more complex and difficult to apply to real subduction zones. Therefore, we preferred to follow a kinematic approach in order to create a simple code adequate to study subduction zones where basic input parameters (age of subducting lithosphere, dip and velocity of subduction) are known.

Our thermo-kinematic model improves some aspects of the above-mentioned works since it includes the main heat sources recognised in subduction zones: adiabatic heating, radioactive heat generation, phase changes and frictional heating. Our model uses, as initial temperature for the lithosphere entering the subduction zone, the thermal plate model GDH1 (Stein and Stein, 1992). Moreover, the model calculates in a self-consistent way the location of the olivine to spinel phase transition, thus permitting the calculation of an accurate distribution of lateral anomalies of density.

3. The model

A thermo-kinematic model is calculated by solving the 2D heat equation given by

$$\left(1+\frac{L_T}{c_P}\frac{\partial\beta}{\partial T}\right)\left(\frac{\partial T}{\partial t}+v_x\frac{\partial T}{\partial x}+v_z\frac{\partial T}{\partial z}\right) = \frac{K}{\rho c_p}\left(\frac{\partial^2 T}{\partial x^2}+\frac{\partial^2 T}{\partial z^2}\right) - v_z\left(\frac{\alpha g}{c_p}T_{abs}+\frac{L_T}{c_p}\frac{\partial\beta}{\partial z}\right)+\frac{H+A_{sh}}{\rho c_p}, \quad (1)$$

where L_T is the latent heat due to the olivine–spinel transformation, c_P is the heat capacity, β is the fraction of spinel, T is the temperature, t is time, x and z are the coordinates, v_x and v_z are the horizontal and vertical components of the velocity, K is the thermal conductivity, ρ is the density, α is the coefficient of thermal expansion, g is the acceleration of gravity, T_{abs} is the absolute temperature, H is the radiogenic heat production rate and A_{sh} is the shear heating rate. The values of the parameters used are listed in Table 1.

Table 1
Definition of parameters common to all calculations

Symbol	Meaning	Value
K	Thermal conductivity	3.2 W m^{-1} K^{-1}
c_p	Specific heat	1.3×10^3 J K^{-1} kg^{-1}
α	Thermal expansion coefficient	3.7×10^{-5} K^{-1}
H	Radiogenic heat production rate (for cont. crust)	8×10^{-7} W m^{-3}
ρ_0	Density of the lithospheric mantle at $T = 0°C$	3400 kg m^{-3}
$\Delta\rho_{ol-sp}$	Density change due to ol–sp phase transition	181 kg m^{-3}
L	Lithospheric thickness	95,000 m
T_0	Temperature at the base of the lithosphere	1450° C
g	Gravitational acceleration	9.8 m s^{-2}
0	Subduction dip angle	60°

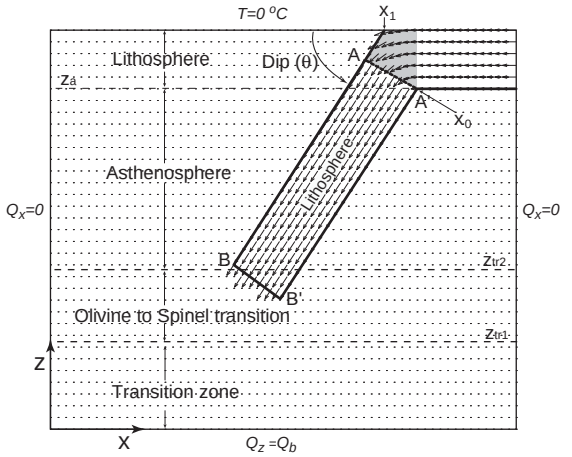

Fig. 1. Schematic diagram illustrating model domain and applied boundary conditions. Velocity field imposed to simulate subduction is updated as slab penetrates into surrounding mantle. Small points indicate nodes of finite difference grid.

The terms on the left-hand side represent the rate of heat change due to the temperature change at a fixed point and advection. The first term on the right-hand side represents heat conduction, the term containing T_{abs} describes the adiabatic heating, that containing L_T represents the latent heat of the olivine to spinel transformation, and the last term accounts for radiogenic and dissipative heating. For simplicity, 'spinel' is here used indistinctly for wadsleyite and/or ringwoodite because of their similar densities.

The model extends vertically to the base of the upper mantle (Fig. 1) where the origin of the vertical coordinate is located. The initial thermal distribution of the oceanic lithosphere is calculated with the thermal plate model GDH1 of Stein and Stein (1992):

$$T_{lit}(z,t') = T_L\left(\frac{z_a+L-z}{L} + \sum_{n=1}^{\infty}\frac{2}{n\pi}\sin\left(\frac{n\pi(z_a+L-z)}{L}\right) \times \exp\left(-\frac{n^2\pi^2 K t'}{\rho c_p L^2}\right)\right), \quad (2)$$

where t' is the time elapsed since the formation of the lithosphere, z_a and T_L indicate location and temperature of the base of the lithospheric plate, and L is the lithospheric thickness. Our code also includes the possibility of simulating continental subduction, with an initial geotherm for the crust and lithospheric mantle given by the steady-state solution of the heat conduction equation

$$T_{crust}(z) = -\frac{H}{K}(z_a+L-z)^2 + \left(\frac{T_L}{L} - \frac{H}{KL}h_c^2 + \frac{2H}{K}h_c\right) \times (z_a+L-z), \quad (3)$$

where h_c is the crustal thickness. This relation assumes constant heat production limited to the crust and a temperature $T = 0°C$ at the surface. The initial temperature for the lithospheric mantle in the continental case is given by

$$T_{lit\ mantle}(z) = \left(\frac{T_L}{L} - \frac{H}{KL}h_c^2\right)(z_a+L-z) + \frac{H}{K}h_c^2. \quad (4)$$

We assume the following adiabatic initial temperature profile for the asthenosphere:

$$T(z) = T_L\exp\left(\frac{g\alpha}{c_p}(z_a-z)\right), \quad z_{tr2} < z \leqslant z_a. \quad (5)$$

We also include a total temperature increase of ΔT, caused by the latent heat released during the olivine to spinel phase change, which initiates at z_{tr2} and is completed at z_{tr1} (see Fig. 1). In this interval the temperature increase is given by (Turcotte and Schubert, 2002)

$$\Delta T = \frac{L_T}{c_p}. \quad (6)$$

We assume that this increase occurs linearly from a temperature T_{ztr2} at z_{tr2} to T_{ztr1} at z_{tr1}:

$$T(z) = \frac{\Delta T}{z_{tr2}-z_{tr1}}(z_{tr2}-z) + T_{ztr2}, \quad z_{tr1} \leqslant z \leqslant z_{tr2}. \quad (7)$$

In the underlying transition zone the initial temperature is given by

$$T(z) = (T_{ztr2}+\Delta T)\exp\left(\frac{g\alpha}{c_p}(z_{tr1}-z)\right), \quad 0 \leqslant z \leqslant z_{tr1}. \quad (8)$$

In order to find the depth at which phase transformations begin and end, we have followed the approach described by Schmeling et al. (1999) and Tezlaff and

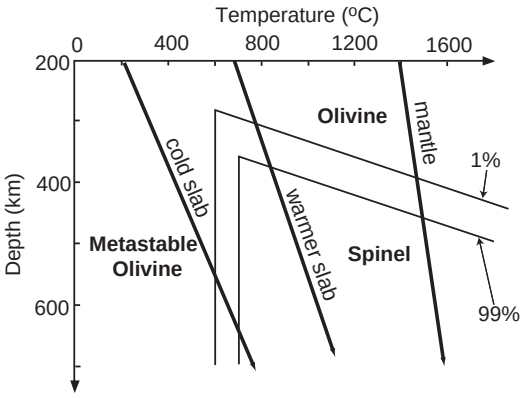

Fig. 2. Simplified disequilibrium (kinetic) phase diagram of olivine–spinel transition showing lines of 1% and 99% spinel fraction as simplified by Schmeling et al. (1999). Thick lines represent characteristic temperature paths within a cold slab, a warmer slab and undisturbed mantle.

Schmeling (2000). Instead of solving the kinetic equations of phase transformation we adopt a simplified phase diagram (Fig. 2). We have incorporated in our modelling the simplified phase diagram of Schmeling et al. (1999) from original data by Akaogi et al. (1989) and Rubie and Ross (1994). The 1% and 99% lines separate the olivine and spinel regimes. The vertical lines represent the transition from metastable olivine into spinel and are only crossed by the geotherms of cold slabs (Fig. 2). The shallower limit of the interval of phase transformation within the undisturbed mantle (z_{tr2}) is given by the intercept between the asthenosphere initial geotherm (Eq. (4)) and the shallower straight line of the phase diagram. z_{tr1} is then obtained by substituting $T_{ztr2} + \Delta T$ into the equation of the phase transition deeper straight line. This diagram is also used to compute the fraction of spinel (β) and its derivatives at any temperature and depth. For the sake of simplicity, β is assumed to change linearly from $\beta = 0$ in the olivine and metastable olivine field to $\beta = 1$ in the spinel field.

We assume the following relation for lateral anomaly of density (with respect to an unperturbed column) due to thermal expansion and phase changes:

$$\Delta\rho = (\rho_0 + \Delta\rho_{ol-sp}\Delta\beta)(1 - \alpha(T - T_0)), \tag{9}$$

where ρ_0 is the density at zero temperature, $\Delta\rho_{ol-sp}$ is the density increase caused by the olivine to spinel phase transition, $\Delta\beta$ is the contrast of fraction of spinel with respect to an unperturbed column with a geotherm T_0. No density changes induced by high pressure–low temperature metamorphism are taken into account.

The applied thermal boundary conditions (Fig. 1) are: $T = 0°C$ at the surface, null horizontal heat flux at the lateral boundaries and constant vertical heat flow at the base of the model. The latter is calculated as the product between the vertical gradient of the initial geotherm at the base of the model and the thermal conductivity.

In our thermo-kinematic approach the velocity field (Fig. 1) is imposed and defined by the subduction velocity v_s and the slab dip θ. In the corner area (shaded in Fig. 1), where the plate begins to dip into the mantle, the velocity field is given by

$$v_x = v_s \frac{z - z_a}{\sqrt{(x - x_0)^2 + (z - z_a)^2}},$$
$$v_z = v_s \frac{x - x_0}{\sqrt{(x - x_0)^2 + (z - z_a)^2}}, \tag{10}$$

where x_0 is the horizontal coordinate of the subduction knee (see Fig. 1). In the subducting slab it is given by

$$v_x = v_s \cos\theta, \quad v_z = v_s \sin\theta. \tag{11}$$

The modelled region is divided into a 2D grid with horizontal and vertical spacing Δx and Δz, with $\Delta x = \Delta z \cos\theta$ in order to force grid nodes to lie on the edges of the slab. At each time step p, the position (B–B′ in Fig. 1) of the bottom edge of the slab (which was located along A–A′ at $t = 0$) is computed, and the slab velocity field (Eq. (11)) is applied to the nodes reached by line B–B′.

We use the following expression (Turcotte and Schubert, 2002) for calculating the shear heating rate:

$$A_{sh} = \tau \frac{v_s}{w} \tag{12}$$

where τ is the shear stress and w is the thickness of the shear zone. Optionally, the code incorporates the procedure proposed by Ponko and Peacock (1995) of distributing shear heating within a $2\Delta x$ wide zone centred on the interface between the slab and the overlying mantle.

The finite difference formulation of the energy equation (Eq. (1)) is developed in Appendix A. We have applied the alternating direction implicit (ADI) method. The resulting equations are solved by applying the Thomas algorithm, as shown in Appendix B. Since the velocity field is updated as the slab penetrates into the mantle, the numerical scheme applied is not stable for every combination of Δt, Δx and Δz, the time step is internally computed by the code in order to ensure stability.

4. Some simulations

We have performed several calculations to show the code behaviour for a wide variety of subduction conditions. Fig. 3 shows the calculated temperatures and the location of the olivine–spinel (1% and 99%) transformation obtained for the cases of slow subduction of a

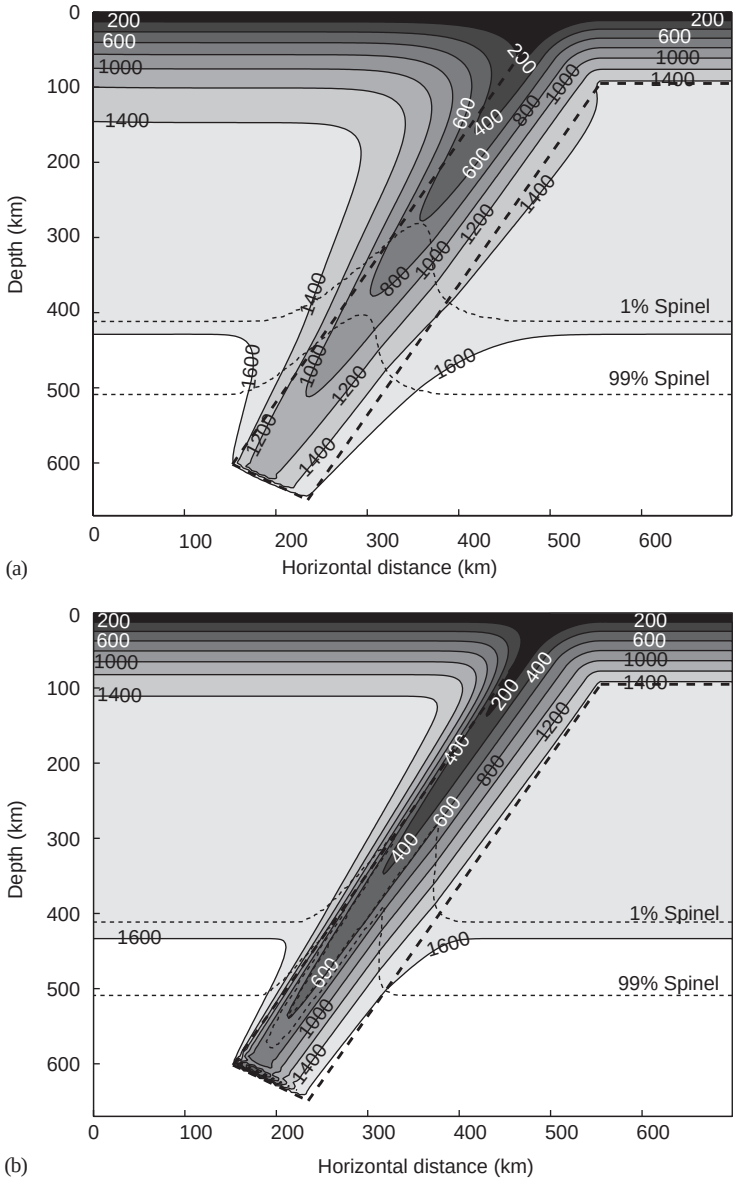

Fig. 3. Temperature (°C, contours every 200°C) distributions calculated with (a) a model of slow subduction of a warm (30 Myr old) oceanic lithosphere after 32 Myr and (b) fast subduction of a cold (120 Myr old) oceanic lithosphere after 6.4 Myr. Subduction velocities are (a) 2 cm year^{-1} and (b) 10 cm yr^{-1}. Position of 1% and 99% olivine–spinel transformation contours are shown by thin dashed lines.

warm (young) oceanic lithosphere and fast subduction of a cold (old) oceanic lithosphere, after 32 and 6.4 Myr of subduction, respectively. Values assumed for the velocity of subduction are 2 and 10 cm yr^{-1} and ages are 30 and 120 Myr, respectively. The values of the thermal parameter ϕ, calculated as the product of the vertical component of the subduction rate and the age of the subducting lithosphere, are 520 and 10,392 km, respectively. A latent heat of phase transformation of $L_T =$ 90 kJ kg^{-1} (Turcotte and Schubert, 2002), and no shear heating or radiogenic production are considered in both cases.

Both models show (Fig. 3) lower temperature in the slab interior with respect to the slab boundaries. Moreover, slabs with high thermal parameters show lower temperatures at fixed depths. Fig. 3 clearly shows the influence of subduction kinematics and pre-subduction thermal state of the lithosphere on the position of the olivine to spinel phase change. In slow and warm subduction zones (Fig. 3a), the phase change is

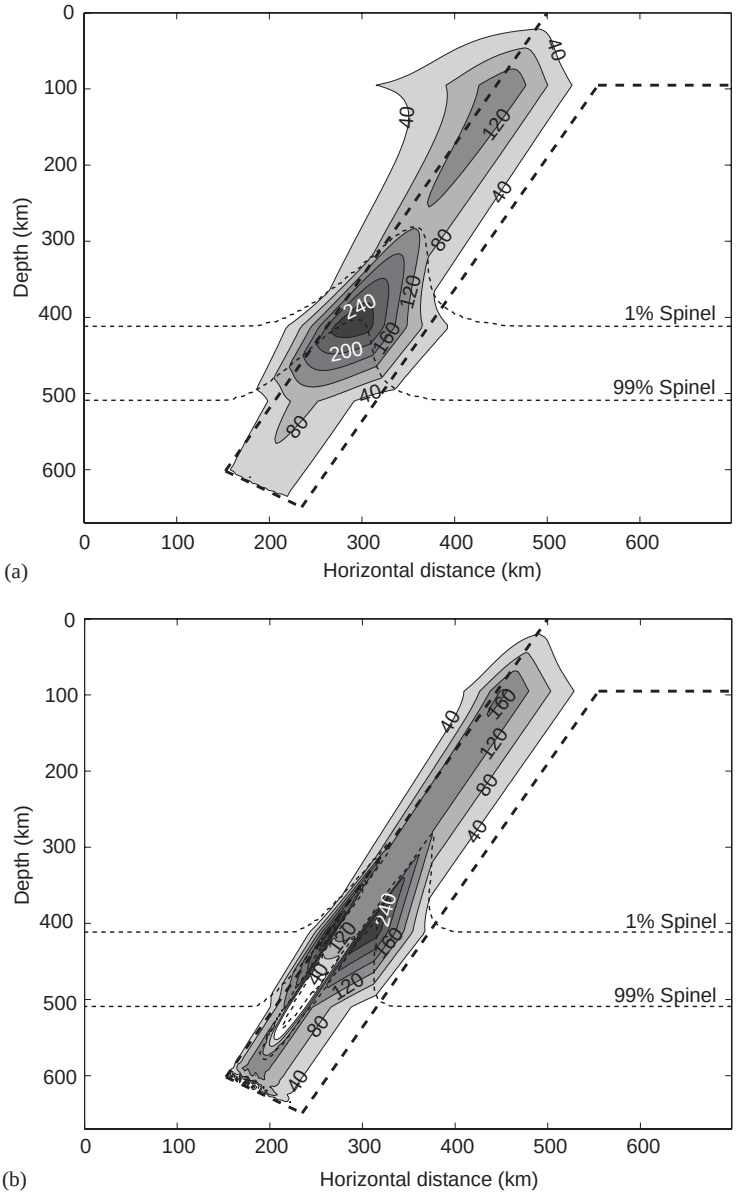

Fig. 4. Lateral anomaly of density (kg m^{-3} contours every 40 km m^{-3}) with respect to right boundary of model domain calculated with (a) a model of slow subduction of a warm (30 Myr old) oceanic lithosphere after 32 Myr and (b) fast subduction of a cold (120 Myr old) oceanic lithosphere after 6.4 Myr. Subduction velocities are (a) 2 cm yr^{-1} and (b) 10 cm yr^{-1}. Position of 1% and 99% olivine–spinel transformation contours are shown by thin dashed lines.

shallower in the slab than in the surrounding mantle, due to depressed isotherms in the slab and to the slope of the equilibrium curve (Fig. 2), and reaches shallowmost depths in the core of the slab. Colder and faster slabs (Fig. 3b) also show a shallowing of the transformation depth within the slab, but the innermost portions of the slab show a deepening of the transition due to the fact that the temperature path in this region enters the metastable olivine field (Fig. 2). In this case, the 600° isotherm, which controls the initiation of metastable olivine to spinel transformation, reaches maximum depths of about 545 km and the conditions for the formation of a wedge of metastable olivine are attained. Deep seismicity is therefore expected to occur for subduction processes with these kinematic and initial thermal conditions.

The distributions of lateral anomalies of density calculated for both models are shown in Fig. 4. Down

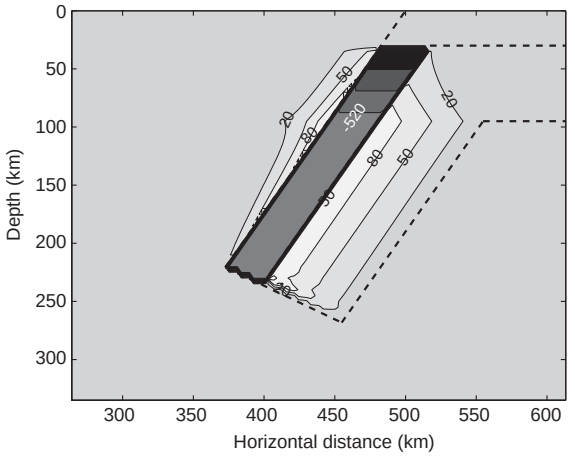

Fig. 5. Lateral anomaly of density (kg m^{-3} contours every 30 km m^{-3}) with respect to right boundary of model domain, after 4 Myr of continental subduction with a velocity of subduction of 5 cm yr^{-1}.

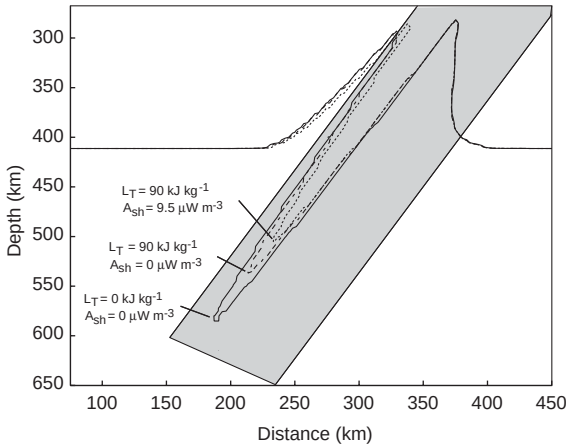

Fig. 6. Influence of latent heat release and shear heating during fast oceanic subduction on depth reached by metastable olivine wedge. Position of 1% olivine–spinel transformation ($\beta = 0.01$) is shown.

to depths of about 300 km, slow slabs show lower densities contrasts than fast slabs, due to higher temperatures. At depths greater than 300–350 km, the shallowing of the olivine to spinel transition within the slab produces a dramatic increase of density in the case of slow subduction of a young plate (Fig. 4a). A negative buoyancy force arises from this positive density contrast. In contrast, it may be noted that the presence of a metastable olivine wedge in cold and fast slabs induces a remarkable lowering of density in the innermost portions of the slabs with respect to the surrounding spinel phase. The resulting positive buoyancy can significantly counteract the negative buoyancy mentioned before, thus producing the so-called 'parachute effect' (Kirby et al., 1996; Schmeling et al., 1999; Tezlaff and Schmeling, 2000).

Fig. 5 shows the lateral anomalies of density resulting from subduction of continental lithosphere, after 4 Myr with a velocity of subduction of 5 cm yr^{-1}. A constant density of 2800 kg m^{-3} has been assumed for a 30 km thick continental crust. For simplicity, we have not included density changes due to metamorphism, but common phase diagrams can be easily incorporated in TEMSPOL. The high negative density anomaly in the subducted crust causes a positive buoyancy force that opposes subduction, which is then only expected to continue if the continental slab is pulled by a deeper oceanic portion of the slab.

Heat sources such as shear heating and latent heat release are often neglected in thermal models of subduction zones. TEMSPOL permits to include such heat sources and to evaluate their contribution to the thermal state of subduction zones. Fig. 6 shows the influence of latent heat and shear heating on the geometry of the metastable olivine wedge, for the model of fast subduction of a cold slab (same parameters as Figs. 3b and 4b). We have considered a shear stress $\tau =$ 30 MPa and a thickness of the shear zone $w = 2\Delta x$, to obtain with Eq. (12) a shear heating rate of $A_{sh} =$ 9.5 μW m^{-3}. We show that neglecting these heat sources can lead to significant overestimation (about 85 km in the case shown in Fig. 5) of the depth reached by the metastable olivine wedge, and thereby of the predicted maximum depth of seismicity.

5. Discussion

We have presented here a code suitable for calculating temperature, mineral phases and density anomaly distribution in deep subduction zones taking into account the olivine–spinel phase transformation in a self-consistent manner. With respect to commonly used thermal models, which neglect shear or radiogenic heating or latent heat released during phase changes, we show that neglecting these heat sources can lead to significant overestimation of the predicted maximum depth of seismicity. Further suitable refinements of the present model are including more complicated phase diagrams and a variable thermal conductivity (Hauck et al., 1999).

Modelling outputs can be used as inputs for numerical simulations which require the knowledge of temperature and density anomaly distributions of subducting zones. For instance, the computed temperature can be used to calculate the brittle and ductile yield stress distribution, assuming a nonlinear rheology, and correlate the obtained stress distribution with observed seismicity

patterns in oceanic and continental slabs (e.g., Carminati et al., 2002). Another possible application relevant for tomography studies is to use the temperature anomalies and temperature derivatives of seismic velocities to obtain the seismic velocity perturbation distribution (e.g., Sleep, 1973; De Jonge et al., 1994; Deal et al., 1999) induced by subduction processes. These synthetic tomographic images can be compared with tomographic models of subduction zones.

The resulting lateral anomaly of density distribution can be introduced into dynamic models assuming either an elastic or viscoelastic rheology (e.g., Bina, 1997; Wittaker et al., 1992; Giunchi et al., 1996; Negredo et al., 1999) to evaluate buoyancy forces and the resulting stress regime and compare it with seismotectonic observations in different subduction zones. Other dynamic effects of the presence of metastable olivine that can be investigated with dynamic models are the change in the velocity of subduction and in the topography of the trench.

Acknowledgements

The authors are very grateful to P. Vacher and an anonymous reviewer for their constructive revision of the manuscript. C. Doglioni is thanked for encouragement and for fruitful discussions. MIUR funding (C. Doglioni) is acknowledged. Spanish research projects Ramón y Cajal, REN2001-3868-C03-02/MAR, and BTE2002-02462 have financially supported this study. Italian MURST 'Progetto Giovani Ricercatori' (E. Carminati) supported this study.

Appendix A. Finite difference formulation of the energy equation

The two-dimensional ADI method is a scheme in which the dependent variable is solved for implicitly in the one direction and then in the other direction at time steps $p+1$ and $p+2$, respectively.

We use the following convention for the grid system:

$$x = i\Delta x, \quad i = 1, 2, \ldots, I,$$
$$z = j\Delta z, \quad j = 1, 2, \ldots, J,$$
$$t = p\Delta t, \quad p = 1, 2, \ldots, P,$$
$$T^p_{i,j} = T^{p\Delta t}_{i\Delta x, j\Delta z}.$$

Consider the finite difference expression of Eq. (1), in which temperature derivatives with respect to x are evaluated at time step $p+1$, and derivatives with respect to z at time step p. At grid point i,j the resulting equation is

$$\begin{aligned} R^p_{i,j}\left(\frac{T^{p+1}_{i,j}-T^p_{i,j}}{\Delta t}+v^p_{xi,j}\frac{T^{p+1}_{i+1,j}-T^{p+1}_{i-1,j}}{2\Delta x}\right.\\ \left.+v^p_{zi,j}\frac{T^p_{i,j+1}-T^p_{i,j-1}}{2\Delta z}\right)\\ =\frac{K}{\rho^p_{i,j}c_p}\left(\frac{T^{p+1}_{i+1,j}-2T^{p+1}_{i,j}+T^{p+1}_{i-1,j}}{\Delta x^2}\right.\\ \left.+\frac{T^p_{i,j+1}-2T^p_{i,j}+T^p_{i,j-1}}{\Delta z^2}\right)\\ -v^p_{zi,j}\left(\frac{L_T}{c_p}\left(\frac{\partial\beta}{\partial z}\right)^p_{i,j}+\frac{\alpha g T^p_{abs\,i,j}}{c_p}\right)\\ +\frac{H_{i,j}+\tau_{i,j}(v_s/w)}{\rho^p_{i,j}c_p}, \end{aligned} \tag{A.1}$$

where

$$R^p_{i,j}=1+\frac{L_T}{c_p}\left(\frac{\partial\beta}{\partial T}\right)^p_{i,j}.$$

After grouping terms Eq. (A.1) becomes

$$A_i T^{p+1}_{i-1,j}+B_i T^{p+1}_{i,j}+C_i T^{p+1}_{i+1,j}=D_i, \tag{A.2}$$

where

$$A_i=-\frac{R^p_{i,j}}{2\Delta x}v^p_{xi,j}-\frac{K}{\rho^p_{i,j}c_p\Delta x^2},$$

$$B_i=\frac{R^p_{i,j}}{\Delta t}+\frac{2K}{\rho^\rho_{i,j}c_p\Delta x^2},$$

$$C_i=\frac{R^p_{i,j}}{2\Delta z}v^p_{zi,j}-\frac{K}{\rho^p_{i,j}c_p\Delta x^2}$$

and

$$\begin{aligned} D_i=&\frac{R^p_{i,j}}{\Delta t}T^p_{i,j}-\frac{R^p_{i,j}}{2\Delta z}v^p_{zi,j}(T^p_{i,j+1}-T^p_{i,j-1})\\ &+\frac{K}{\rho^p_{i,j}c_p\Delta z^2}(T^p_{i,j+1}-2T^p_{i,j}+T^p_{i,j-1})\\ &-v^p_{zi,j}\left(\frac{L_T}{c_p}\left(\frac{\partial\beta}{\partial z}\right)^p_{i,j}+\frac{\alpha g T^p_{absi,j}}{c_p}\right)+\frac{H^p_{i,j}+\tau^p_{i,j}(v_s/w)}{\rho^p_{i,j}c_p}. \end{aligned}$$

An equation similar to Eq. (A.2) is obtained at each point in the jth row, yielding a set of I equations. This set of equations gives the temperature at $p+1$ at each point of the jth row in terms of variables known at the time step p. We apply the Thomas' algebraic scheme to solve this set of equations (see Appendix B).

We now consider the finite difference formulation of Eq. (1) in which temperature derivatives with respect to x are evaluated at time $p+1$, and derivatives with

respect to z at time $p+2$:

$$R^p_{i,j}\left(\frac{T^{p+2}_{i,j}-T^{p+1}_{i,j}}{\Delta t}+v^p_{xi,j}\frac{T^{p+1}_{i+1,j}-T^{p+1}_{i-1,j}}{2\Delta x}+v^p_{zi,j}\frac{T^{p+2}_{i,j+1}-T^{p+2}_{i,j-1}}{2\Delta z}\right)=\frac{K}{\rho^p_{i,j}c_p}\left(\frac{T^{p+1}_{i+1,j}-2T^{p+1}_{i,j}+T^{p+1}_{i-1,j}}{\Delta x^2}+\frac{T^{p+2}_{i,j+1}-2T^{p+2}_{i,j}+T^{p+2}_{i,j-1}}{\Delta z^2}\right)-v^p_{zi,j}\left(\frac{L_T}{c_p}\left(\frac{\partial\beta}{\partial z}\right)^{p+1}_{i,j}+\frac{\alpha g T^{p+1}_{absi,j}}{c_p}\right)+\frac{H^p_{i,j}+\tau^p_{i,j}(v_s/w)}{\rho^p_{i,j}c_p} \quad (A.3)$$

which, grouping terms, gives

$$A_jT^{p+2}_{i,j-1}+B_jT^{p+2}_{i,j}+C_jT^{p+2}_{i,j+1}=D_j, \quad (A.4)$$

where

$$A_j=-\frac{R^p_{i,j}}{2\Delta z}v^p_{xi,j}-\frac{K}{\rho^p_{i,j}c_p\Delta z^2},$$

$$B_j=\frac{R^p_{i,j}}{\Delta t}+\frac{2K}{\rho^p_{i,j}c_p\Delta z^2},$$

$$C_j=\frac{R^p_{i,j}}{2\Delta z}v^p_{zi,j}-\frac{K}{\rho^p_{i,j}c_p\Delta z^2}$$

and

$$D_j=\frac{R^p_{i,j}}{\Delta t}T^{p+1}_{i,j}-\frac{R^p_{i,j}}{2\Delta x}v^p_{xi,j}(T^{p+1}_{i+1,j}-T^{p+1}_{i-1,j})+\frac{K}{\rho^p_{i,j}c_p\Delta x^2}(T^{p+1}_{i+1,j}-2T^{p+1}_{i,j}+T^{p+1}_{i-1,j})-v^p_{zi,j}\left(\frac{L_T}{c_p}\left(\frac{\partial\beta}{\partial z}\right)^{p+1}_{i,j}+\frac{\alpha g T^{p+1}_{abs\,i,j}}{c_p}\right)+\frac{H^p_{i,j}+\tau^p_{i,j}(v_s/w)}{\rho^p_{i,j}c_p}.$$

An equation of form (A.4) can be obtained for each point of the ith column, yielding J simultaneous equations. The I sets of J equations obtained at time $p+2$ are solved as before applying the Thomas algorithm (Appendix B). Therefore, the temperature at time $p+2$ is obtained from temperature at time p in two time steps. An equation implicit in x (Eq. (A.2)) is used for the first time step and an equation implicit in z (Eq. (A.4)) for the second.

Appendix B. Application of Thomas' algorithm to the ADI scheme of the energy equation

We consider the system of equations obtained at time step $p+1$:

$$A_iT_{i-1,j}+B_iT_{i,j}+C_iT_{i+1,j}=D_i, \quad i=1,2,\ldots,I-1, \quad (B.1)$$

where we are omitting the superscripts. The Thomas algorithm operates by reducing this system of equations to upper triangular form, by eliminating T_{i-1} in each of the equations. Consider that the first k equations (B.1) have been reduced to

$$T_{i,j}-w_iT_{i+1,j}=g_i, \quad i=1,2,\ldots,k, \quad (B.2)$$

the last of these equations is

$$T_{k,j}-w_kT_{k+1,j}=g_k \quad (B.3)$$

and the next equation in the original form is

$$A_{k+1}T_{k,j}+B_{k+1}T_{k+1,j}+C_{k+1}T_{k+1,j}=D_{k+1}. \quad (B.4)$$

We eliminate $T_{k,j}$ from (B.3) and (B.4) and rearrange terms

$$T_{k+1,j}-\frac{-C_{k+1}}{B_{k+1}+A_{k+1}w_k}T_{k+2,j}=\frac{D_{k+1}-A_{k+1}g_k}{B_{k+1}+A_{k+1}w_k} \quad (B.5)$$

comparison with Eq. (B.2) shows that the coefficients w_i and g_i can be obtained from the following recurrence relations:

$$w_i=\frac{-C_i}{B_i+A_iw_{i-1}} \quad g_i=\frac{D_i-A_ig_{i-1}}{B_i+A_iw_{i-1}} \quad i=2,3,\ldots,I. \quad (B.6)$$

The initial values can be obtained by applying in Eq. (B.2) the condition of zero horizontal heat flow at the lateral boundaries, $T_{1,j}=T_{2,j}$, then

$$w_1=1, \quad g_1=0. \quad (B.7)$$

We use these initial values to recursively find all the coefficients. Then we can calculate the last value of T by applying again the boundary condition $T_{I,j}=T_{I-1,j}$ in Eq. (B.2):

$$T_{I,j}=\frac{g_{I-1}}{1-w_{I-1}}. \quad (B.8)$$

Therefore, beginning from the known value of $T_{I,j}$, Eq. (B.2) gives the values $T_{I-1,j}$, $T_{I-2,j}$, in order, finishing with $T_{1,j}$. This computation is stable if $|w_i|<1$.

In the following time step, $p+2$, the temperature derivatives with respect to z are evaluated at $p+2$, and derivatives with respect to x at time $p+1$. We now apply the boundary conditions at the base and surface of the model. We assume constant basal heat flow Q_b to obtain

$$T_{i,2}=T_{i,1}-\frac{Q_b}{K}\Delta z. \quad (B.9)$$

We then apply Eq. (B.2)

$$T_{i,1} - w_1\left(T_{i,1} - \frac{Q_b}{K}\Delta z\right) = g_1, \qquad \text{(B.10)}$$

so if $w_1 = 1$, then $g_1 = (Q_b/K)\Delta z$. We then apply Eq. (B.6) to find recursively the rest of the coefficients. Finally, with the condition of constant surface temperature of 0°C, so $T_{i,J} = 0$, we can apply Eq. (B.2) to calculate $T_{i,J-1}, \ldots, T_{i,1}$.

References

Akaogi, M., Ito, E., Navrotsky, L., 1989. Olivine-modified spinel–spinel transitions in the system $Mg_2SiO_4 - Fe_2SiO_4$: calorimetric measurements, thermochemical calculation and geophysical application. Journal of Geophysical Research 94, 15671–15685.

Bina, C.R., 1996. Phase transition buoyancy contributions to stresses in subducting lithosphere. Geophysical Research Letters 23, 3563–3566.

Bina, C.R., 1997. Patterns of deep seismicity reflect buoyancy stresses due to phase transitions. Geophysical Research Letters 24, 3301–3304.

Carminati, E., Giardina, F., Doglioni, C., 2002. Rheological control on subcrustal seismicity in the Apennines subduction (Italy). Geophysical Research Letters 29, doi:10.1029/2001GL014084.

Dässler, R., Yuen, D.A., 1996. The metastable olivine wedge in fast subducting slabs; constraints from thermo-kinetic coupling. Earth and Planetary Science Letters 137, 109–118.

Deal, M., Nolet, G., Van der Hilst, R.D., 1999. Slab temperature and thickness from seismic tomography. Journal of Geophysical Research 104, 28789–28802.

De Jonge, M.R., Wortel, M.J.R., Spakman, W., 1994. Regional scale tectonic evolution and the seismic velocity structure of the lithosphere and upper mantle: the Mediterranean region. Journal of Geophysical Research 99, 12091–12108.

Devaux, J.P., Schubert, G., Anderson, C., 1997. Formation of a metastable olivine wedge in a descending slab. Journal of Geophysical Research 102, 24627–24637.

Devaux, J.P., Fleitout, L., Schubert, G., Anderson, C., 2000. Stresses in a subducting slab in the presence of a metastable olivine wedge. Journal of Geophysical Research 105, 13365–13373.

Frohlich, C., 1989. The nature of deep focus earthquakes. Annual Review of Earth and Planetary Sciences 17, 227–254.

Giunchi, C., Sabadini, R., Boschi, E., Gasperini, P., 1996. Dynamic models of subduction: geophysical and geological evidence in the Tyrrhenian Sea. Geophysical Journal International 126, 555–578.

Green, H.W., Young, T.E., Walker, D., Scholz, C.H., 1990. Anticrack-associated faulting at very high pressure in natural olivine. Nature 348, 720–722.

Hauck, S.A. II, Phillips, R.J., Hofmeister, A.M., 1999. Variable conductivity: effects on the thermal structure of slabs. Geophysical Research Letters 26, 3257–3260.

Kirby, S.H., Durham, W.B., Stern, L.A., 1991. Mantle phase changes and deep-earthquake faulting in subducting lithosphere. Science 252, 216–225.

Kirby, S.H., Stein, S., Okal, E., Rubie, D.C., 1996. Metastable mantle phase transformations and deep earthquakes in subducting oceanic lithosphere. Reviews of Geophysics 34, 261–306.

Marton, F.C., Bina, C.R., Stein, S., Rubie, D.C., 1999. Effects of slab mineralogy on subduction rates. Geophysical Research Letters 26, 119–122.

McKenzie, D.P., 1969. Speculations on the consequences and causes of plate motions. Geophysical Journal of the Royal Astronomical Society 188, 1–32.

Meade, C., Jeanloz, R., 1991. Deep-focus earthquakes an recycling of water into the Earth's mantle. Science 252, 68–72.

Minear, J.W., Toksöz, M.N., 1970. Thermal regime of a downgoing slab and new global tectonics. Journal of Geophysical Research 75, 1397–1419.

Negredo, A.M., Carminati, E., Barba, S., Sabadini, R., 1999. Dynamic modelling of stress accumulation in Central Italy. Geophysical Research Letters 26, 1945–1948.

Ponko, S.F., Peacock, S.M., 1995. Thermal modelling of the southern Alaska subduction zone: insight into the petrology of the subducting slab and overlying mantle wedge. Journal of Geophysical Research 100, 22117–22128.

Rubie, D.C., 1984. The olivine–spinel transformation and the rheology of subducting lithosphere. Nature 308, 505–508.

Rubie, D.C., Ross, C.R., 1994. Kinetics of the olivine–spinel transformation in subducting lithosphere: experimental constraints and implications for deep slab process. Physics of Earth and Planetary Interiors 86, 223–241.

Schmeling, H., Monz, R., Rubie, D.C., 1999. The influence of olivine metastability on the dynamics of subduction. Earth and Planetary Science Letters 165, 55–66.

Scholz, C.C.H., 1990. The Mechanics of Earthquakes and Faulting, Cambridge University Press Cambridge, UK, 439pp.

Sleep, N.H., 1973. Teleseismic P-wave transmission through slabs. Bulletin of the Seismological Society of America 63, 1349–1373.

Stein, C.A., Stein, S., 1992. A model for the global variation in oceanic depth and heat flow with lithospheric age. Nature 359, 123–129.

Stein, S., Stein, C.A., 1996. Thermo-mechanical evolution of oceanic lithosphere: implications for the subduction process and deep earthquakes. Subduction from top to bottom. Geophysical Monograph 95, 1–17.

Tezlaff, M., Schmeling, H., 2000. The influence of olivine metastability on deep subduction of oceanic lithosphere. Physics of Earth and Planetary Interiors 120, 29–38.

Toksöz, M.N., Minear, J.W., Julian, B.R., 1971. Temperature field and geophysical effects of a downgoing slab. Journal of Geophysical Research 76, 1113–1138.

Turcotte, D.L., Schubert, G., 1973. Frictional heating of the descending lithosphere. Journal of Geophysical Research 78, 5876–5886.

Turcotte, D.L., Schubert, G., 2002. Geodynamics, 2nd Edition. Cambridge University Press, Cambridge, UK, 456pp.

Wittaker, A., Bott, M.H.P., Waghorn, G.D., 1992. Stress and plate boundary forces associated with subduction plate margins. Journal of Geophysical Research 97, 11933–11944.